# Accepted Manuscript

# A force sensor based on three weakly coupled resonators with ultrahigh sensitivity

Chun Zhao[a,*], Graham S. Wood[a], Jianbing Xie[b], Honglong Chang[b], Suan Hui Pu[a,c], Michael Kraft[d,**]

[a]*Nano Research Group, School of Electronics and Computer Science, University of Southampton, Southampton SO17 1BJ, UK*
[b]*MOE Key Laboratory of Micro and Nano System for Aerospace, Northwestern Polytechnical University, 127 Youyi West Road, Xi'an 710072, Shaanxi, China*
[c]*University of Southampton Malaysia Campus, Nusajaya, 79200 Johor, Malaysia*
[d]*University of Liege, Montefiore Institute, Grande Traverse 10, 4000 Liege, Belgium*

## Abstract

A proof-of-concept force sensor based on three degree-of-freedom (DoF) weakly coupled resonators was fabricated using a silicon-on-insulator (SOI) process and electrically tested in $20\mu$Torr vacuum. Compared to the conventional single resonator force sensor with frequency shift as output, by measuring the amplitude ratio of two of the three resonators, the measured force sensitivity of the 3DoF sensor was $4.9 \times 10^6$/N, which was improved by two orders magnitude. A bias stiffness perturbation was applied to avoid mode aliasing effect and improve the linearity of the sensor. The noise floor of the amplitude ratio output of the sensor was theoretically analyzed for the first time, using the transfer function model of the 3DoF weakly coupled resonator system. It was shown based on measurement results that the output noise was mainly due to the thermal-electrical noise of the interface electronics. The output noise spectral density was measured, and agreed well with theoretical estimations. The noise floor of the force sensor output was estimated to be approximately 1.39nN for an assumed 10Hz bandwidth of the output signal, resulting in a dynamic range of 74.8dB.

---

[*]Corresponding author
[**]Principle corresponding author
*Email address:* cz1y10@ecs.soton.ac.uk (Chun Zhao)
*URL:* http://www.ecs.soton.ac.uk/people/cz1y10 (Chun Zhao)

## 1. Introduction

For the last couple of decades, emerging micro- and nano-scale devices enabled the measurement of forces in the region of pN to $\mu$N. Measurement of the forces in this range plays important roles in many different areas, including sur-
5 face characterization [1], contact potential difference measurement [2], study of biomechanics [3] and cell mechanobiology [4], inertial sensing [5], manipulation of microscale objects [6] and magnetometer for electronic compass [7], among many others.

Among these miniature force sensors, resonant sensing devices are attractive
10 to researchers due to its quasi-digital output signal and high accuracies [8]. The conventional approach employs a single degree-of-freedom (DoF) resonator; when an external force is exerted on the resonator, the stiffness changes while the mass remains the same, leading to a frequency shift [9]. The challenge to improve the performance of the force sensor, aiming to sense smaller forces
15 motivates research in alternative sensing paradigms.

One promising approach, which couples two identical resonators with a spring much weaker than that of the resonators, is to form a 2DoF system [10]. This approach utilizes a *mode localization* effect which was first described in solid-state physics by Anderson [11]. When a small perturbation is applied
20 on one of the resonators, the mode shapes of the system change. It was demonstrated that by measuring the eigenstates shift caused by mode localization, orders of magnitude improvement in sensitivity of mass change was observed [10]. Various groups demonstrated that orders of magnitude enhancement in sensitivity of stiffness change [12, 13, 14, 15] and force [16] could be achieved
25 using this approach. Another advantage of this type of device is its intrinsic common mode rejection [17].

The force to be measured can be applied to a resonator in different direc-

2

tions, depending on the application: one way is to apply a vertical force or force gradient to the tip of a horizontal cantilever, as demonstrated in [18]. This ap-
30 proach is widely used for atomic force microscopy (AFM) due to its simplicity. However, for non-contact AFM applications, when the gradient of the Van der Waals force exceeds the stiffness of the cantilever, snap-down instability occurs [19], which is analogous to the pull-in effect occurring in parallel plate actuation. Hence, a large stiffness for the vibrating structure is required for some appli-
35 cations, which, in turn, deteriorates the force sensitivity and resolution of the sensor. To reach maximum stability while not compromising the sensitivity, an alternative method is to apply the force along the length of a beam [20, 21]. Due to a relatively high longitudinal stiffness of a beam, the instability is alleviated [21].

40 In this work, a novel proof-of-concept force sensor consisting of three res- onators with enhanced force sensitivity is presented. The reason for using a 3DoF resonator system is that, the third resonator located in between two iden- tical resonators reduces the energy propagation due to its absorption of energy, thus increases the energy attenuation along the chain. Consequently, it enhances
45 the mode localization when a structural disorder is present. It has been demon- strated in both theory and by measurement results [22, 23] that a 3DoF weakly coupled resonator sensor can exhibit enhanced sensitivity compared to existing 2DoF mode-localized sensors. The device was fabricated using a silicon-on- insulator process, and tested electrically. The external force was an quasi-static
50 electrostatic force applied along the direction of the beam length, which avoided the potential instability mentioned above. The 3DoF force sensor utilized the mode shape change due to a stiffness perturbation introduced by an external force. The vibration amplitude ratio of two resonators at one mode of interest was used to measure the mode shape change. Two orders of magnitude im-
55 provement in sensitivity, compared to 1DoF resonator sensors with frequency shift as an output signal, was observed from the measurement. In addition to sensitivity, resolution and dynamic range of the force sensing device is also discussed.

3
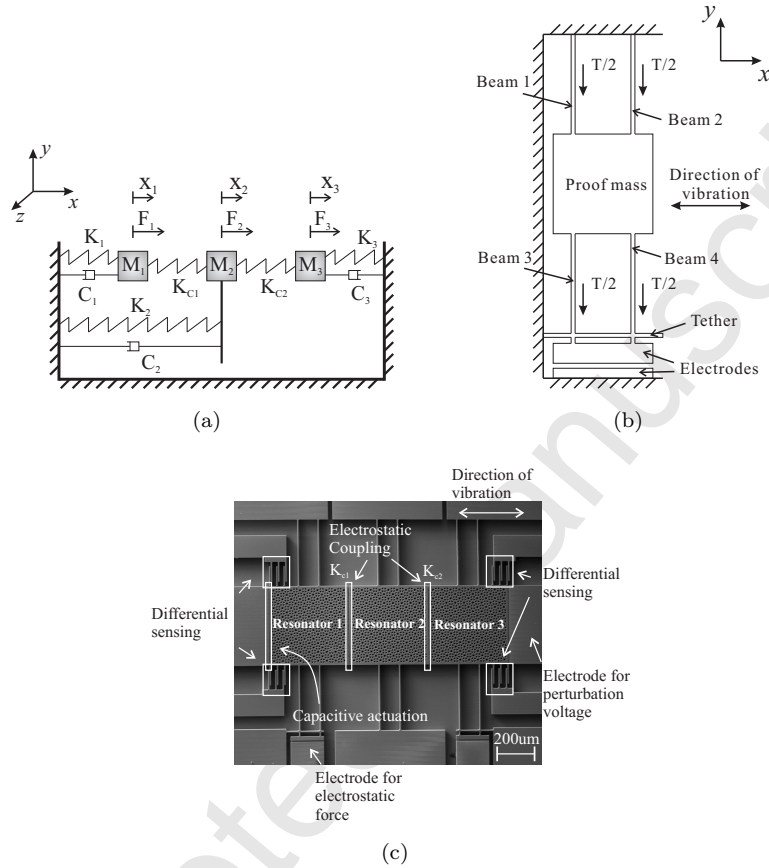
Figure 1: Figures showing: a) block diagram of a 3DoF resonator sensing device [15]; b) a detailed schematic diagram of the left resonator to which the force is applied; and c) SEM image of the fabricated 3DoF resonator force sensor.

## 2. Theory

### 2.1. Force sensing mechanism

To understand the behaviour of the 3DoF resonator force sensor, the system is modelled as a lumped parameter block diagram as shown in Fig. 1a. A schematic drawing of the left resonator to which the force to be measured is applied, is shown in Fig. 1b, and a SEM image of our proof-of-concept chip is shown in Fig. 1c.

4

A tether structure [24] was used in our design to allow the transmission of an axial electrostatic force to the suspension beams of the left resonator. In addition, it is also used to impede the movement of the electrode attached to the bottom of the suspension beams when the resonator is vibrating, so that the electrostatic force is kept as constant as possible. Therefore, the tether was made wide in the $x$-axis ($170\mu$m), but thin in the $y$-axis ($5\mu$m) in our design.

The design ensures that the tether has a high mechanical stiffness in the $x$-direction. In addition, when the displacement of the resonator in the direction of vibration is small compared to the length of the beam, the movement of the resonator in the $y$-axis is negligible. Consequently, the tether efficiently constraints the movement of the electrode attached to the suspension beams, and thus it can also be regarded as a fixed end for the two suspension beams attached.

In the $y$-axis, the tether, which is a cantilever beam in essence, has a stiffness of [25]:

$$K_{\text{tether}} = \frac{Etw_t^3}{4L_t^3} \tag{1}$$

where $E, t, w_t, L_t$ are the Young's modulus, the thickness of the device, the width in the $y$-axis and effective length of tether, respectively. The longitudinal stiffness of the suspension beam is given by [25]:

$$K_{\text{long}} = \frac{Etw}{L} \tag{2}$$

where $w$ and $L$ are the width in the $x$-axis and the length of the suspension beam.

To applied forces in the negative $y$-direction, the tether and the suspension beams act similarly to two springs in parallel [24]. Ideally, the tether does not absorb any force applied in the $y$-axis, so that all the forces can be measured by the resonator. For our design, the shortest effective length of the tether is $60\mu$m, resulting in a maximum stiffness of $K_{\text{tether}} = 538$N/m. Whereas in the $y$-axis, suspension beams 1 and 3 are in series, therefore the effective longitudinal

5

stiffness is $K_{\text{long}} = 2.48 \times 10^4 \text{N/m}$. This indicates that more than 97.9% of the force applied is absorbed by the suspension beams, with less than 2.1% of the force exerting on the tether. Hence, we are able to assume that the entire electrostatic force is transmitted to the resonators for measurement.

When two different DC voltages are applied to the resonator and the electrode below, an electrostatic force is generated in the negative $y$-axis pulling the resonator. Due to the relatively large length of the electrode in the $x$-axis of $160\mu$m compared to the air gap of $4.5\mu$m, the fringe field can be neglected. Assuming small displacements in the $y$-axis, the tensile force for the resonator $T$ in terms of voltage difference $\Delta V$ between the resonator and the electrode, cross-sectional area of electrode $A_e$, air gap $d_e$ and dielectric constant of vacuum $\varepsilon_0$ is given by [25]:

$$T = \frac{\varepsilon_0 A_e \Delta V^2}{2 d_e^2} \tag{3}$$

For an applied force in the $y$-axis, the two identical suspension beams (beams 3 and 4 in Fig. 1b), are in parallel. Hence the tensile force $T$ is evenly distributed to the two suspension beams. Furthermore, the suspension beams 1 and 3 are in series, so are suspension beams 2 and 4. Therefore, the tensile force applied on each suspension beam equals to $T/2$.

The suspension beams have one end fixed, while the other end moves perpendicular with respect to the beam length. Given the displacement functions along the axis of the beam for these boundary conditions [26], the stiffness of each suspension beam under weak axial tensile force $T/2$ is given by [27]:

$$K_{\text{beam}} = \frac{Etw^3}{L^3} + \frac{0.6T}{L} \tag{4}$$

Moreover, due to the high longitudinal stiffness of the suspension beams, the elongation of the beams are trivial compared to the beam length $L$. For a tensile force of $1\mu$N, the resulting elongation of the beams is less than 0.1nm, which is negligible compared to the beam length of $300\mu$m; the strain change is therefore neglected. The stiffness perturbation introduced by the tensile force,

6

normalized to the effective stiffness of the resonator $K$, is therefore:

$$\frac{\Delta K_{\text{force}}}{K} = \frac{2.4T}{LK} \tag{5}$$

With the coupling voltage $V_c$ applied, suppose $d$ is the air gap between
120 parallel plates and $A, A_{cf}$ are the cross-sectional area of the actuation parallel plate and the comb finger overlap, respectively. Neglecting the intrinsic tension introduced during fabrication process, the effective stiffness is given by [15]:

$$
\begin{aligned}
K &= 4 \times K_{\text{beam}} - K_{\text{elec}} \\
&= \frac{4Etw^3}{L^3} - \frac{\varepsilon_0(A + 6A_{cf})V_c^2}{d^3}
\end{aligned} \tag{6}
$$

*2.2. Amplitude ratio*

In the model of the 3DoF force sensor, as shown in Fig. 1a, each resonator
125 consists of a mass, spring and damper, and is coupled to its neighbouring resonator through springs ($K_{c1}$ and $K_{c2}$).

Suppose the mass of all resonators and their corresponding coupling spring stiffness are identical, i.e., $M_1 = M_2 = M_3 = M$ and $K_{c1} = K_{c2} = K_c$, while the spring stiffness of the resonators are asymmetrical with a quasi-static stiffness
130 perturbation of $\Delta K$, thus $K_3 = K + \Delta K$, $\Delta K < 0$ and $K_1 = K$, and the stiffness of the resonator in the middle is different to the other two resonators with $K_2 \neq K$. The damping coefficients are included due to its constraints on the value of $\Delta K$ (as will be shown in Section 2.3), and it will be used in later sections for noise considerations. Further, assuming all springs are linear, and
135 no movement in the $y$ and $z$-axis, the motion in the $x$-direction of the resonators can be described by the equations of motion of the system (Eqs. (A.1) to (A.3) in Appendix A).

Now, consider the case where the coupled resonator system is only driven by $F_1(s) = F_1$ and $F_2(s) = F_3(s) = 0$, the frequencies of the in-phase and

7

140 out-of-phase modes can be calculated, and are given by [23]:

$$\omega_{\mathrm{ip}} \approx \sqrt{\frac{1}{M}\left[K + K_c + \frac{1}{2}(\Delta K - \alpha - \sqrt{\Delta K^2 + \alpha^2})\right]} \qquad (7)$$

$$\omega_{\mathrm{op}} \approx \sqrt{\frac{1}{M}\left[K + K_c + \frac{1}{2}(\Delta K - \alpha + \sqrt{\Delta K^2 + \alpha^2})\right]} \qquad (8)$$

Where

$$\alpha = \frac{2K_c^2}{K_2 - K + K_c} \qquad (9)$$

Let $s = j\omega$, and substitute the out-of-phase mode frequency (Eq. (8)) into the equations of the transfer functions of $|H_{11}(j\omega)|$ (Eq. (A.12)) and $|H_{31}(j\omega)|$ (Eq. (A.17)), for the system driven only by $F_1$, the amplitude ratios of the

145 out-of-phase modes can be approximated as:

$$\left|\frac{X_1(j\omega_{\mathrm{op}})}{X_3(j\omega_{\mathrm{op}})}\right| \approx \left|-\frac{\sqrt{\gamma_3^2(\Delta K/K)^2 + 4} - \gamma_3(\Delta K/K)}{2} + j\frac{\gamma_3}{Q}\right| \qquad (10)$$

Where

$$\gamma_3 = \frac{2K}{\alpha} = \frac{K(K_2 - K + K_c)}{K_c^2} \qquad (11)$$

With a tensile force applied on resonator 1, the stiffness of resonator 1 is increased by a positive $\Delta K_{\mathrm{force}}$. When the tensile force is weak, so that $\Delta K_{\mathrm{force}} \ll K$, this is equivalent to break the symmetry of the resonator system

150 with a negative stiffness perturbation $-\Delta K_{\mathrm{force}}$ acting on resonator 3. Therefore, we are able to gauge an external force applied along the beam length of the resonator, by measuring the amplitude ratio change resulting from a stiffness change caused by the force.

### 2.3. Mode aliasing effect

155 Damping has the effect that it lowers the quality factor of the vibration modes, therefore limiting the bandwidth of the modes. If the in-phase and out-of-phase modes overlap, this effect is termed mode aliasing. Hence, for a

8

given bandwidth $\Delta f_{3\mathrm{dB}}$ of the modes, the two main modes having a frequency difference of $\Delta f$ do not alias, the following antialiasing condition has to be satisfied:

$$\Delta f > 2 \times \Delta f_{3\mathrm{dB}} \tag{12}$$

With the frequencies of the in-phase and out-of-phase modes given by Eqs. (7) and (8), the frequency difference can be approximated as:

$$\Delta f = f_{\mathrm{op}} - f_{\mathrm{ip}} \approx \frac{1}{2\pi}\sqrt{\frac{K}{M}}\sqrt{\left(\frac{\Delta K}{2K}\right)^2 + \left(\frac{1}{\gamma_3}\right)^2} \tag{13}$$

It can be seen from Eq. (13) that the frequency difference is a function of the stiffness perturbation $\Delta K$. Hence, small stiffness perturbations $\Delta K$ can result in a frequency difference $\Delta f$ violating the condition of Eq. (12); and thus strong mode aliasing would occur. This is illustrated by a simulation using an equivalent RLC electrical circuit model of the 3DoF weakly coupled resonator system [28]. The values used in the simulation are chosen to be close to the device design, and are listed in Table 1.

Table 1: Values used for the simulations to demonstrate mode aliasing

| Component | Values | Mechanical model equivalent |
|---|---|---|
| $L$ | 0.489MH | $M$ |
| $C$ | 0.254fF | $K$ |
| $C_2$ | 84.8aF | $K_2/K = 3$ |
| $C_c$ | -19.07fF | $K/K_c = -75, \gamma_3 = 11174$ |
| $R$ | 8.77M$\Omega$ | $Q = 5000$ |
| $\Delta C$ | a) 0fF | $\Delta K = 0$ |
| | b) $-0.17$pF | $\Delta K/K = -1.5 \times 10^{-3}$ |

It can be seen from Fig. 2 that for $\Delta K = 0$ strong mode aliasing occurs, which stops the sensor from functioning properly by preventing the observer

9

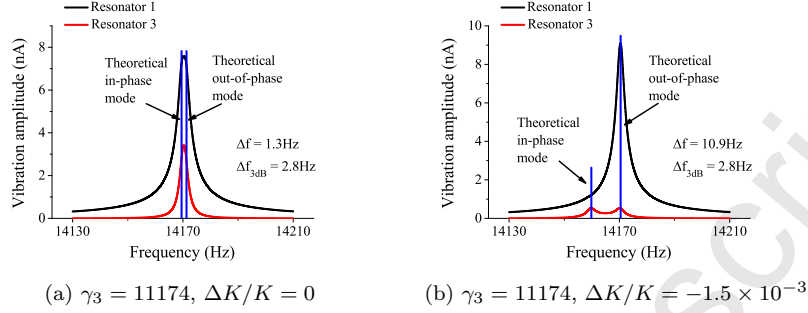(a) $\gamma_3 = 11174$, $\Delta K/K = 0$      (b) $\gamma_3 = 11174$, $\Delta K/K = -1.5 \times 10^{-3}$

Figure 2: Simulated frequency responses of resonators 1 and 3 using an equivalent electrical RLC network model [28] with different stiffness perturbations: a) $\gamma_3 = 11174$, $\Delta K/K = 0$ and b) $\gamma_3 = 11174$, $\Delta K/K = -1.5 \times 10^{-3}$. The theoretically calculated frequency difference and the 3dB bandwidth of the modes are also shown in the figure. Strong mode aliasing can be seen in a), as the in-phase and the out-of-phase modes merged; this is due to the frequency difference violating the anti-aliasing condition (Eq. (12)). The mode aliasing effect reduces to a negligible level when the anti-aliasing condition is satisfied, and the two modes can be distinguished in b).

from identifying the out-of-phase mode. On the contrary, when the anti-aliasing condition is satisfied for $\Delta K/K = -1.5 \times 10^{-3}$, the out-of-phase mode can be distinguished, and the amplitude ratio can be measured. Hence, it is important
175 that the anti-aliasing condition Eq. (12) is satisfied for all input conditions.

### 2.4. Nonlinearity of amplitude ratio

It can be seen from the amplitude ratio expression (Eq. (10)) that the amplitude ratio is a nonlinear function of the normalized stiffness perturbation $\Delta K/K$. Mathematically, it can be further deduced that for large $|\Delta K/K|$, the
180 amplitude ratio approaches a linearized scale function of $\Delta K/K$:

$$\left| \frac{X_1(j\omega_{\mathrm{op}})}{X_3(j\omega_{\mathrm{op}})} \right| \approx \left| \frac{\gamma_3 \Delta K}{K} \right| \tag{14}$$

It can be seen from Eq. (10) that two nonlinearity errors contribute to the total nonlinearity error: a) a nonlinearity from the first term occurring even without damping and b) a nonlinearity due to damping (term $j\gamma_3/Q$). By

10

calculating the nonlinearity errors separately and superimposing, we are able to

185 estimate the total nonlinearity error, $\epsilon$, as:

$$\epsilon = \epsilon_1 + \epsilon_2 \approx \left(\frac{K}{\gamma_3 \Delta K}\right)^2 + \frac{1}{2}\left(\frac{1}{Q}\frac{K}{\Delta K}\right)^2 \tag{15}$$

where $\epsilon_1$ is the nonlinearity error from the first term and $\epsilon_2$ is the nonlinearity error from the second term. To verify this estimation, a simulation using the equivalent RLC electrical circuit model is run using the values listed in Table 2. The stiffness perturbations used in the simulations complied with the anti-

190 aliasing condition.

Table 2: Values used for the simulations to verify the nonlinearity error estimation

| Component | Values | Mechanical model equivalent |
|-----------|--------|-----------------------------|
| $L$ | 0.489MH | $M$ |
| $C$ | 0.254fF | $K$ |
| $C_2$ | 84.8aF | $K_2/K = 3$ |
| $R$ | 8.77M$\Omega$ | $Q = 5000$ |
| $C_c$ | a) -12.72fF | $K/K_c = -50, \gamma_3 = 4950$ |
| | b) -19.07fF | $K/K_c = -75, \gamma_3 = 11174$ |

The results shown in Fig. 3 showed good agreement between the theoretical estimations and the simulated results of the nonlinearity error. It can also be seen from the figure that the nonlinearity error diminished as the value of the negative $\Delta K/K$ decreased. Hence, in order to improve the linearity of the

195 amplitude ratio, it is desired to have a high stiffness perturbation.

*2.5. Bias point*

To ensure that any tensile force applied will not result in severe mode alias-ing, a negative bias stiffness perturbation $\Delta K_{\text{bias}} < \Delta K_{\text{max}} < 0$ can be applied to resonator 3; this is depicted in Fig. 4. With this bias perturbation, for
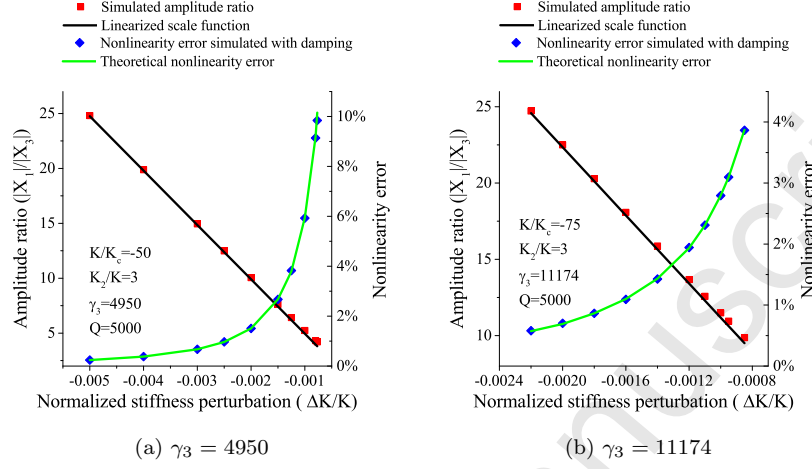
11

(a) $\gamma_3 = 4950$

(b) $\gamma_3 = 11174$

Figure 3: Simulated amplitude ratios compared to the linearized scale function given by Eq. (14). The total nonlinearity errors were also calculated and are plotted for a) $\gamma_3 = 4950$ and b) $\gamma_3 = 11174$. The total theoretical nonlinearity error was estimated using Eq. (15). The nonlinearity errors determined by simulation match the theoretical predictions well.

200   $\Delta K_{\text{force}} > 0$ resulting from a tensile force, the total stiffness perturbation $\Delta K$ satisfies $\Delta K = \Delta K_{\text{bias}} - \Delta K_{\text{force}} < \Delta K_{\text{max}}$.

In addition, the negative bias stiffness perturbation also makes $\Delta K = \Delta K_{\text{bias}} - \Delta K_{\text{force}} < -\Delta K_{\text{force}}$, hence, the nonlinearity of the amplitude ratio is also decreased; this is also shown in Fig. 4.

205   To introduce the negative stiffness perturbation bias, we applied a DC voltage on the electrode on the right, hence lowering the effective stiffness of resonator 3. Once an appropriate bias stiffness perturbation (which will be discussed in Section 4.2) is introduced, the mode aliasing effect and nonlinearity can be made negligible. Therefore Eq. (10) can be linearized as Eq. (14).

210   Combining Eqs. (5) and (14) and neglecting the nonlinearity, the change in amplitude ratio is approximately linear with the tensile force, $T$:

$$\Delta \left| \frac{X_1(j\omega_{\text{op}})}{X_3(j\omega_{\text{op}})} \right| \approx \frac{\gamma_3 \Delta K_{\text{force}}}{K} = \frac{2.4\gamma_3 T}{KL} \qquad (16)$$
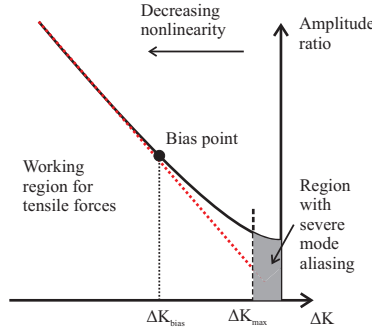
12

Figure 4: Demonstration of the bias point concept. The amplitude ratio as a function of the stiffness perturbation is based on an analytical model described in the previous sections. The black curve shows the actual curve of amplitude ratio, the red dotted line shows the linearized scale function and the grey area illustrates the region with severe mode aliasing. It demonstrates that with a bias point outside the region with strong mode aliasing, the working region for tensile forces will not suffer from the same effect. It also shows that improved linearity can be achieved through deploying a bias point.

Therefore, the sensitivity of the force sensor can be approximated as:

$$\mathcal{S}_{3DoF} = \frac{\partial(\text{Amplitude ratio})}{\partial T} \approx \frac{2.4\gamma_3}{KL} \tag{17}$$

With the bias, the lower limit of the dynamic range of the quasi-static force is only limited by the noise floor of the sensor and the interface electronics.

215 Hence, we shall discuss the noise in the following section.

*2.6. Noise*

Assuming the noise of the sensing device is Gaussian and the noise of resonator 1 and 3 are not correlated, the output noise power of the 3DoF sensor, equivalent to the variance of the amplitude ratio $|X_1/X_3|$, can be derived ac-

220 cording to [29]:

$$\left|\frac{X_1}{X_3}\right|^2_{\text{noise}} = \sigma^2\left(\left|\frac{X_1}{X_3}\right|\right)$$
$$= \left|\frac{X_1}{X_3}\right|^2 \left[\left(\frac{\sigma(X_1)}{X_1}\right)^2 + \left(\frac{\sigma(X_3)}{X_3}\right)^2\right]$$

13

$$= \left| \frac{X_1}{X_3} \right|^2 \left[ \frac{X_{n,1}^2}{X_1^2} + \frac{X_{n,3}^2}{X_3^2} \right] \tag{18}$$

where $\sigma^2(f)$ is the variance of function $f$, which by definition equals to the noise power; $X_{n,i}^2$ ($i = 1, 3$) is the noise power of the $i$th resonator. Hence the signal-to-noise ratio (SNR) is:

$$\text{SNR} = \left| \frac{X_1}{X_3} \right|^2 \Big/ \left| \frac{X_1}{X_3} \right|_{\text{noise}}^2 = \left( \frac{X_{n,1}^2}{X_1^2} + \frac{X_{n,3}^2}{X_3^2} \right)^{-1}$$
$$= \frac{\text{SNR}_1 \times \text{SNR}_3}{\text{SNR}_1 + \text{SNR}_3} \tag{19}$$

It can be seen from Eq. (19) that the output SNR increases as the SNR of
225    resonator 1 and/or 3 improves.

The noise power of resonator 1 and 3 is dominated by two parts, mechanical-thermal noise of the resonators and the electrical-thermal noise of the interface electronics [30]. Therefore, the SNR of resonator 1 and 3 can be written as:

$$\text{SNR}_i = \frac{\text{SNR}_{m,i} \times \text{SNR}_{e,i}}{\text{SNR}_{m,i} + \text{SNR}_{e,i}}, \quad i = 1 \text{ or } 3 \tag{20}$$

where $\text{SNR}_{m,i}$ and $\text{SNR}_{e,i}$ are the mechanical and electrical SNR of the $i$th
230    resonator, respectively.

*2.6.1. Mechanical SNR*

To theoretically calculate the mechanical noise, a transfer function model [15] of the 3DoF resonator sensor was used. The block diagram of the model is shown in Fig. 5.
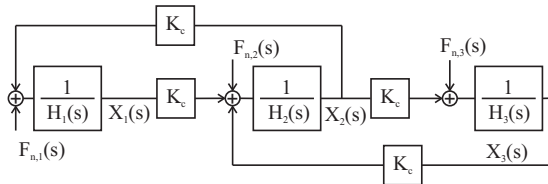


Figure 5: Block diagram of a 3DoF resonator sensing device

14

235    Considering three mechanical-thermal noise inputs $F_{n,r}$ ($r = 1$ to 3) (see Fig. 5), the noise power in terms of displacement near the out-of-phase mode of the $r$th resonator $X_{mn,i}$ ($i = 1$ to 3) can be evaluated as [31]:

$$X_{mn,i}^2 = \frac{1}{2\pi} \int_{\omega_{op}-\Delta\omega}^{\omega_{op}+\Delta\omega} \sum_{r=1}^{3} F_{n,r}^2 H_{ir}^2 \mathrm{d}\omega \tag{21}$$

Where $H_{ir}$ is the transfer function from $r$th input to $i$th output, which is derived in Appendix A, and the power spectral density of the thermal driving 240   force is given by [32, 30]:

$$F_{n,r}^2 = 4k_B T C_r, \quad r = 1, 2, 3 \tag{22}$$

Where $k_B, T$ and $C_r$ are the Boltzmann constant, ambient temperature and damping coefficient of $r$th resonator, respectively.

Suppose $C_1 = C_2 = C_3 = C$, the noise power of the displacement of resonator 1 is:

$$X_1^2 = \frac{2k_B T C}{\pi} \int_{\omega_{op}-\Delta\omega}^{\omega_{op}+\Delta\omega} (H_{11}^2 + H_{12}^2 + H_{13}^2) \mathrm{d}\omega \tag{23}$$

245    Assume a quality factor of $Q = 2 \times 10^4$ in vacuum, which is a conservative estimation compared to other similar devices [12, 33] and setting $|K/K_c| = 200$, $K_2/K = 2$, $\gamma_3$ can be calculated to be 40000 using Eq. (11). The sensor, without any force applied, has a bias of $|\Delta K_{\mathrm{bias}}/K| = 5/\gamma_3$. As shown in Appendix B, it can be demonstrated that near the out-of-phase mode, $|H_{12}|^2$ and $|H_{13}|^2$ are 250   both negligible compared to $|H_{11}|^2$. Therefore Eq. (23) can be simplified as:

$$X_1^2 \approx \frac{2k_B T C}{\pi} \int_{\omega_{op}-\Delta\omega}^{\omega_{op}+\Delta\omega} H_{11}^2(j\omega) \mathrm{d}\omega \tag{24}$$

Based on the integrals derived in [34], we are able to estimate the spectral density of the thermal-mechanical noise displacement of resonator 1, $\langle X_1(j\omega_{op})\rangle^2$, in close vicinity of the out-of-phase mode, assuming $\Delta\omega \ll \omega_{op}$, as:

$$\langle X_1(j\omega_{op})\rangle^2 \approx \frac{8k_B T C Q^2}{K^2} \tag{25}$$

15

Furthermore, for $\Delta\omega = \omega_{op}/(2Q)$, the mechanical SNR of resonator 1 within the 3dB bandwidth of the out-of-phase mode can be evaluated as:

$$\mathrm{SNR}_{m,1} \approx \frac{X_1^2(j\omega_{op})K_{\mathrm{eff}}}{k_B T} \tag{26}$$

In a similar manner, the noise displacement power spectral density at the out-of-phase mode $\langle X_3(j\omega_{op})\rangle^2$ and the mechanical SNR of resonator 3 can be approximated by:

$$\langle X_3(j\omega_{op})\rangle^2 \approx \frac{8k_B TCQ^2}{K^2}\frac{X_1^2(j\omega_{op})}{X_3^2(j\omega_{op})} \tag{27}$$

$$\begin{aligned}\mathrm{SNR}_{m,3} &\approx \frac{X_3^2(j\omega_{op})K_{\mathrm{eff}}}{2\pi k_B T}\frac{X_1^2(j\omega_{op})}{X_3^2(j\omega_{op})} \\ &\approx \frac{X_1^2(j\omega_{op})K_{\mathrm{eff}}}{k_B T}\end{aligned} \tag{28}$$

*2.6.2. Electrical SNR*

For a standard transimpedance amplifier, the input-referred current noise power spectral density can be expressed as [31]:

$$i_n^2 = i_{na}^2 + \left(\frac{R_m + R_f}{R_m R_f}\right)^2 e_{na}^2 + \left(\frac{4k_B T}{R_f}\right)^2 \tag{29}$$

where $i_{na}, e_{na}, R_m$ and $R_f$ are the current noise, voltage noise spectral density of the op-amp, equivalent motional resistance of the resonator and feedback resistance, respectively. Given the sensing transduction factor $\eta_s$ [25] of the device and the 3dB bandwidth of the out-of-phase mode $f_{3dB}$, the electrical SNR of resonator 1 and 3 within the 3dB bandwidth can therefore be calculated as:

$$\mathrm{SNR}_{e,i} = \frac{X_i^2\eta_s^2}{i_{n,i}^2 f_{3dB}}, \quad i = 1 \text{ or } 3 \tag{30}$$

As will be shown in the experimental results, for a biased 3DoF resonator sensor, within the 3dB bandwidth, for resonator 1 with larger vibration amplitude, the mechanical noise from the resonators is the dominant noise source, whereas outside of the bandwidth, the total noise was mainly attributed to the

16

electronic noise. But for resonator 3 having a smaller vibration amplitude, the electrical noise dominated. The ultimate limit of the output noise power was imposed by electrical noise from the interface electronics.

## 3. Experiment

### 3.1. Device description

To demonstrate the concept of a 3DoF force sensor, a device was fabricated using a single mask silicon on insulator (SOI) process [35] with a structural layer of $30\mu$m thickness. The fabrication process for the device is described in detail elsewhere [15].

The design of this chip is different from our previous work [15]. In this device, the beam width was $4\mu$m (compared to $5\mu$m, which was the stated minimum width for good yield). In addition, the length of the beams were $300\mu$m, the resulting aspect ratio of the beam was 75, higher than the previous device of 70. This demonstrates the potential capability of the process to fabricate compliant beams. With these dimensions, the spring constant of the resonators was weaker for the device tested in this work, which is desirable for sensitivity improvement.

Moreover, the air gap was reduced to $3.5\mu$m to achieve higher actuation and sensing transduction factors. With smaller air gaps, the DC voltage required to achieve a certain coupling strength is also lowered. One downside of smaller air gap is the increased electrostatic nonlinearity, which contributes to a the nonlinear sensitivity, as discussed later.

The design parameters of the fabricated device are listed in Table 3.

### 3.2. Measurement methodology

To electrically test the chip, the chip was mounted on a chip carrier and wire bonded to the contacts. The chip carrier was then inserted into a socket on a printed circuit board. The circuit board was placed into a customized vacuum chamber with electrical feedthroughs. The ambient pressure was $20\mu$Torr ensuring minimum air damping loss, so a high quality factor could be obtained.
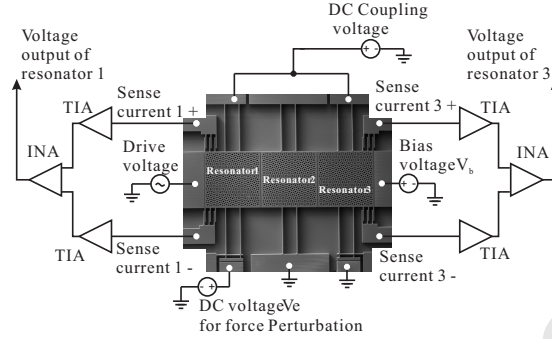
17

Figure 6: Test configuration of the prototype 3DoF resonator sensing device

Three DC voltages were used in the experiment: a) a fixed coupling voltage of
300 $V_c = 12$V was applied to resonators 1 and 3, while resonator 2 was grounded,
hence the resonators were electrostatically coupled; b) a variable voltage $V_b$, the
value of which will be discussed later, was used to bias the 3DoF sensor to an
appropriate operating point; c) a variable voltage $V_e < 0$ was used to apply
a tensile force on resonator 1. With the voltages applied, suppose $A_c$ and $d_c$
305 are the cross-sectional area and the air gap between resonators, the coupling
strength is given by [25]:

$$K_c = -\frac{\varepsilon_0 A_c V_c^2}{d_b^3} \tag{31}$$

Similarly, given that $A_b$ and $d_b$ are the cross-sectional area and the air gap
between the electrode on the right and resonator 3, the bias stiffness $\Delta K_{\text{bias}}$ is
given by:

$$\Delta K_{\text{bias}} = -\frac{\varepsilon_0 A_b (V_c - V_b)^2}{d_b^3} \tag{32}$$

310 It should be noted that the same configuration was used for resonator 3.
Therefore, when the electrode for resonator 3 was grounded as demonstrated in
Fig. 6, and $V_e < 0$ applied for perturbation on resonator 1, using Eq. (3), the
effective perturbation force can be calculated as:

18

$$\Delta T = \frac{\varepsilon_0 A_e[(V_c - V_e)^2 - V_c^2]}{2d_e^2}$$
$$= \frac{\varepsilon_0 A_e(V_e^2 - 2V_cV_e)}{2d_e^2} \tag{33}$$

The resulting perturbation is therefore:

$$\frac{\Delta K_{\text{force}}}{K} = \frac{2.4\Delta T}{LK} = \frac{1.2\varepsilon_0 A_e(V_e^2 - 2V_cV_e)}{KLd_e^2} \tag{34}$$

315    Motional currents were used to measure the motion of resonators 1 and 3. With both resonators vibrating at the same frequency, the ratio of the motional currents equals to the amplitude ratio. Standard TIAs (AD8065, Analog Devices Inc) with feedback resistance of 6.6MΩ were used to convert and amplify the differential motional currents to differential voltage signals, which were

320    further amplified by subsequent instrumentation amplifiers (INAs) (AD8421, Analog Devices Inc) with a differential gain of 100. The sub-nano ampere motional currents from the resonators were amplified to voltages at a measurable level of hundreds of millivolts, whereas the common mode signals such as the feedthrough signals, were suppressed to the sub-millivolt range.

325    A two-channel oscilloscope (DSO6032A, Agilent Technologies) was used for measuring the voltage amplitudes of the resonators simultaneously. By manually altering the frequency of the drive signal, which was generated from a signal generator with variable frequency function, in 0.01Hz steps, two distinct peaks in the amplitudes could be found, i.e., the in-phase and out-of-phase modes. The

330    out-of-phase mode was used in our measurement for high sensitivity, which was identified by the phase difference between the resonators. Then, the applied frequency was maintained at the out-of-phase mode frequency for the oscilloscope to measure the amplitudes in over 500 cycles. The oscilloscope computed the mean value of the amplitudes of both resonators, which were then used to calcu-

335    late the amplitude ratios. Additionally, the mode frequencies were recorded as displayed by the signal generator. It is worth noting here that the third mode was neglected in the analysis due to the fact that in the experiment this mode

19

could not be detected as the amplitudes of resonators 1 and 3 were below the noise level.

340   ## 4. Results and discussion

### 4.1. $\gamma_3$ and offset values extraction

Before proceeding to demonstrate the force sensor, $\gamma_3$ and stiffness offset values were extracted due to their importance in analysing the experimental results [15].

345   The 3dB bandwidth of the out-of-phase mode was found to be 0.48Hz, the quality factor was 28653 (as shown in Fig. 9). While ensuring the mode aliasing effect was negligible and with $V_e$ kept at 0V, bias voltage $V_b$ was altered to change $\Delta K/K$. The amplitude ratios were recorded for different $\Delta K/K$, and the amplitude ratio curve was fitted to Eq. (10), as shown in Fig. 7. The extracted

350   values of $\gamma_3 = 29119$ and the offset in normalized stiffness offset $= 5.16 \times 10^{-4}$. Compared to the theoretically calculated value of $\gamma_3 = 39557$ from the designed dimensions, the relative error is approximately 26%, this is due to the variances introduced during the fabrication process.
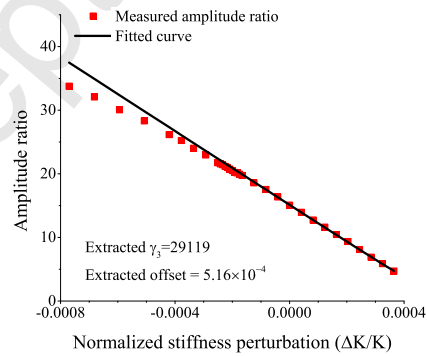


Figure 7: Measured amplitude ratios (in red dots) were fitted to Eq. (10) to extract $\gamma_3$ and offset value in normalized stiffness perturbation. The fitted curve is shown in black. The extracted $\gamma_3 = 29119$ and offset $= 5.16 \times 10^{-4}$.
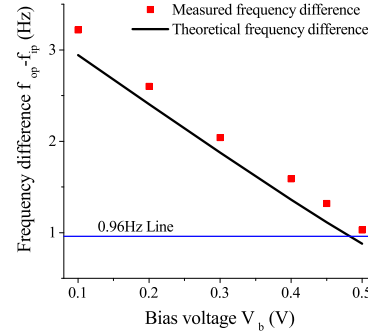
20

Figure 8: Measured (red) and theoretically calculated (black) frequency difference as a function of the bias voltage $V_b$. The theoretical frequency differences were calculated using equation Eqs. (7) and (8) with $\gamma_3$, offset value extracted and the designed dimensions. $2f_{3dB} = 0.96$Hz is marked with a blue line in the figure. Measured frequency differences match well with theoretical calculated values. It can also be seen that for bias voltages smaller than 0.5V, the anti-aliasing condition was satisfied.

### 4.2. Bias point selection

A bias stiffness perturbation $\Delta K_{\text{bias}}$ was intentionally introduced in the experiment, in order to avoid the mode aliasing effect. This was achieved by applying a fixed bias voltage $V_b$, as shown in Fig. 6. To reduce the mode aliasing effect, the anti-aliasing condition, Eq. (12), should be satisfied.

A mode frequency measurement was carried out to find the range of the bias voltage $V_b$ that satisfies Eq. (12). The results are shown in Fig. 8. Since the 3dB bandwidth of the in-phase and out-of-phase modes were 0.48Hz from the measurement, the minimum frequency difference that satisfies Eq. (12) was 0.96Hz, which was marked with a blue line in Fig. 8. Therefore, a bias voltage of $V_b \leq 0.5$V satisfied the anti-aliasing condition.

Moreover, as mentioned in Section 2.4, a negative $\Delta K_{\text{bias}}$ with larger magnitude, therefore, a lower $V_b$ (refer to Eq. (32)), is desired for better linearity. However, as shown from Eq. (18), a larger $|\Delta K|$ leads to a larger $|X_1/X_3|$, hence leading to larger noise in the amplitude ratio. Therefore, to balance the trade-off, $V_b = 0.4$V was used for perturbation. The corresponding normalized

21

370  stiffness perturbation $\Delta K_{\mathrm{bias}}/K$ and amplitude ratio were $1.91 \times 10^{-4}$ and 5.75, respectively.
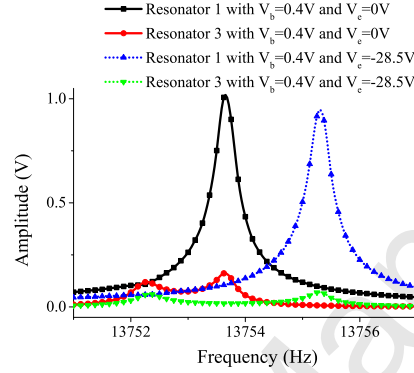
## 4.3. Force measurement



Figure 9: Measured frequency response of resonator 1 and 3 under two different perturbation conditions: a) $V_b = 0.4$V and $V_e = 0$V, shown in solid lines; b) $V_b = 0.4$V and $V_e = -28.5$V, shown in dotted lines. The quality factor was calculated to be 28653.

To demonstrate the functionality of the proof-of-concept force sensing device, electrostatic forces along the beam length were created by applying $V_e$ to the
375  electrode for resonator 1. With $V_e < 0$ applied, a tensile force was exerted on resonator 1, therefore decreasing $\Delta K$. Hence the frequency difference $\Delta f$ increased and the mode aliasing effect could be neglected, as shown in Fig. 9. It can also be seen from Fig. 9 that negligible spring nonlinearity was present; therefore the assumption of linear springs can be regarded as valid.

380  Varying $V_e$, we were able to measure the amplitude ratios. Using Eq. (33), the effective tensile forces applied were calculated. Hence, we can obtain the theoretical amplitude ratio using Eqs. (10) and (34). Fig. 10 shows the measured amplitude ratios and linearized scale function, given by Eq. (16), together with the nonlinearity error. It can be seen from Fig. 10 that the measured am-
385  plitude ratio matched well with the linearized scale function, with a nonlinearity error smaller than 10% for all the data points. The linear force sensitivity was found to be $4.9 \times 10^6$/N. The theoretical force sensitivity is calculated to be

22

$6.6 \times 10^6/\text{N}$. The relative error compared to theoretical prediction is $-26\%$, which is attributed to fabrication tolerances.
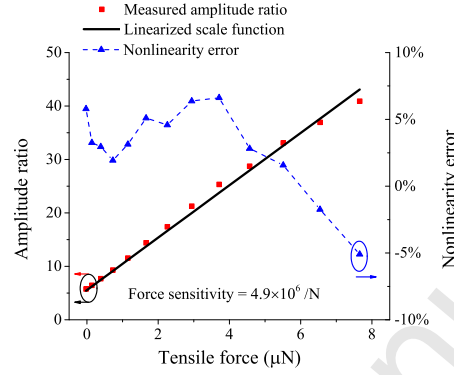


Figure 10: Measured amplitude ratios and the linearized scale function with respect to the applied tensile force. The measured amplitude ratios matched well with the linearized scale function, with nonlinearity error smaller than 10% for all the data points. The force sensitivity is found to be $4.9 \times 10^6/\text{N}$.

A comparison of sensitivity to other state-of-the-art resonant force sensors are listed in Table 4. It can be seen that significant improvement in sensitivity of at least two to three orders of magnitude was achieved.

*4.4. Force resolution and dynamic range*

Since any motion caused by mechanical noise (SNR given by Eqs. (26) and (28)) went through the same amplification stages on the printed circuit board, the output mechanical SNR of the $i$th resonator is therefore:

$$\text{SNR}_{m,i} = \frac{V_i^2 K_{\text{eff}}}{k_B T (2\omega_{op}\eta_s R_f G_{\text{INA}})^2}, \quad i = 1 \text{ or } 3 \tag{35}$$

where $V_i$ is the rms-value of the output voltage of the $i$th resonator and $G_{\text{INA}}$ are the differential gain of the instrumentation amplifiers.

From Eqs. (29) and (30), the electrical SNR at the output can be computed as:

$$\text{SNR}_{e,i} = \frac{V_i^2}{(\sqrt{2}i_{n,i}R_f G_{\text{INA}})^2}, \quad i = 1 \text{ or } 3 \tag{36}$$
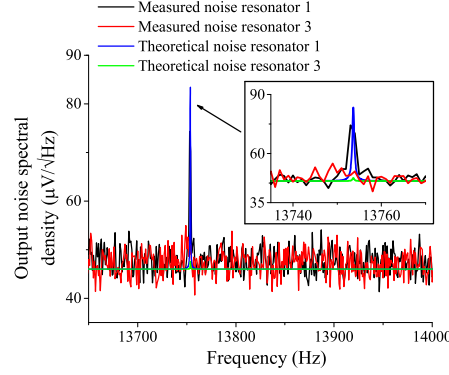
23

Figure 11: Output voltage noise spectral density of resonator 1 and 3 compared to the theoretically estimated noise density. The measured noise floor agreed well with theoretical calculations.

The noise spectral density was measured using a two channel dynamic signal analyser (35670A by Agilent Technologies) without any driving signals applied, while $V_c = 12$V, $V_b = 0.4$V and $V_e = 0$V were retained. Averaging of 50 measurement results were used to reduce the measurement variation, hence the peak caused by the mechanical noise could be found. The theoretical noise was calculated using Eqs. (35) and (36), together with the equations in section 2.6. It can be seen from Fig. 11 that the measurement results and theoretical predictions agreed well. Therefore we were able to evaluate the noise power based on the theoretical noise.

Assuming an ambient temperature of 290K, using the designed value of the sensing transduction factor, $\eta_s$ from Table 3, $R_f = 6.6$M$\Omega$ and $G_{\mathrm{INA}} = 100$ as designed, when $V_b = 0.4$V and $V_e = 0$V, resulting in an amplitude ratio $|X_1/X_3| = 5.75$, the SNRs can be calculated from the noise power within 3dB bandwidth ($f_{3dB} = 0.48$Hz) using the measured output signal. The evaluated SNR and noise power are listed in Table 5.

It can be seen from Table 5 that the electrical noise of resonator 3 (the resonator with smaller amplitude) ultimately sets the noise floor of the amplitude ratio. Due to the fact that the thermal-electrical noise can be regarded as uni-

24

formly distributed in a wide frequency span, as a consequence, the amplitude
ratio noise can also be regarded as white noise. Therefore, from Table 5, we can
evaluate the minimum resolvable force of the sensor near the bias point as:

$$
\begin{aligned}
\langle T \rangle_{min} &= \frac{\langle \text{Amplitude ratio} \rangle_{min}}{\text{Force sensitivity}} \\
&= \frac{\sqrt{2.23 \times 10^{-6}/0.48}}{4.9 \times 10^6} \text{N}/\sqrt{\text{Hz}} \\
&= 4.40 \times 10^{-10} \text{N}/\sqrt{\text{Hz}}
\end{aligned}
\tag{37}
$$

where $\langle \text{Amplitude ratio} \rangle_{min}$ is the evaluated noise power spectral density
of the amplitude ratio, hence, the frequency bandwidth in Eq. (37) is the
bandwidth of the output voltage signals.

To estimate the dynamic range of the 3DoF sensor, a bandwidth of 10Hz
of the output voltage signal was supposed; for this assumption, the minimum
detectable DC force is 1.39nN. For a maximum force of 7.6$\mu$N in the experiment,
a dynamic range of approximately 74.8dB can be achieved.
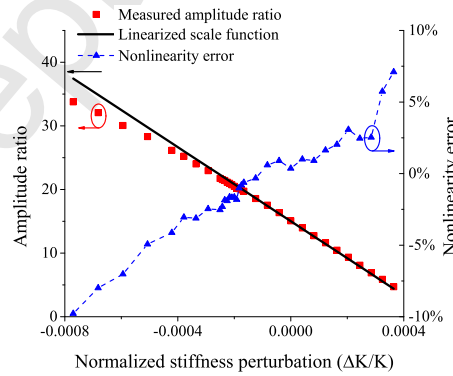
### 4.5. Nonlinearity



Figure 12: Measured amplitude ratio and the linearized scale function (Eq. (14)) as a function
of normalized stiffness perturbation. Nonlinearity error was also calculated and shown in the
figure. Nonlinearity error decreased in value as the amplitude ratio increased.

430    From the measurement results, it can be noticed that the nonlinearity error of the 3DoF device started off decreasing in value as the amplitude ratio increased, as shown in Fig. 12, which agreed with the theoretical prediction in Section 2.4.

However, the linearity of the 3DoF sensor tended to deteriorate as the amplitude ratio increased, as shown in Figs. 10 and 12. It should be noticed that

435 this nonlinearity was found to be insignificant for the device in [15]. One possible reason for this is that the air gap between the resonators was $3.5\mu$m in this design, smaller compared to $4.5\mu$m in [15]. For example, when amplitude of resonator 1 is significantly higher than resonator 3 (larger than 30 times), the nonlinearity of $K_{c1}$ becomes larger than that of $K_{c2}$, making the assumption of

440 $K_{c1} = K_{c2}$ invalid for larger amplitude ratios.

## 5. Summary and future work

In this work, a proof-of-concept force sensing device consisting of three weakly coupled resonators with enhanced sensitivity is reported. Two orders of magnitude improvement in sensitivity compared to current state-of-the-art

445 resonant force sensors was observed. A noise floor of the output signal, i.e. for 10Hz bandwidth of the output signal, 1.39nN could be demonstrated.

Currently the measurement method requires mode frequency searching, which makes real-time measurement of a fast changing force impossible. Hence, only quasi-static stiffness and force perturbations were used as inputs. Future work

450 will include the design of a self-oscillating loop that is capable of locking to a particular mode of interest. This would enable the measurement of the dynamic inputs.

Furthermore, since the resonators were coupled by electrostatic forces, in a future study we can completely switch off the coupling voltages to decouple the

455 resonators. This would enable a better comparison between the 3DoF and the 1DoF resonator sensor in the future.

26

## Appendix A. Transfer function derivation

The motion of the three resonators can be described by three differential equations:

$$M\ddot{x}_1 + C_1\dot{x}_1 + (K + K_c)x_1 - K_c x_2 = F_1 \qquad (A.1)$$

$$M\ddot{x}_2 + C_2\dot{x}_2 + (K + 2K_c)x_2 - K_c x_1 - K_c x_3 = F_2 \qquad (A.2)$$

$$M\ddot{x}_3 + C_3\dot{x}_3 + (K + \Delta K + K_c)x_3 - K_c x_2 = F_3 \qquad (A.3)$$

460   where $x_i, F_i$ denote the displacement of the proof mass with respect to a fixed frame and external force on the mass of the $i$th resonator ($i = 1, 2, 3$), respectively. After performing a Laplace transformation and rearranging, we obtain:

$$H_1(s)X_1(s) = K_c X_2(s) + F_1(s) \qquad (A.4)$$

$$H_2(s)X_2(s) = K_c X_1(s) + K_c X_3(s) + F_2(s) \qquad (A.5)$$

$$H_3(s)X_3(s) = K_c X_2(s) + F_3(s) \qquad (A.6)$$

where the transfer functions are defined as:

$$H_1(s) \equiv Ms^2 + C_1 s + (K + K_c) \qquad (A.7)$$

$$H_2(s) \equiv Ms^2 + C_2 s + (K_2 + 2K_c) \qquad (A.8)$$

$$H_3(s) \equiv Ms^2 + C_3 s + (K + K_c + \Delta K) \qquad (A.9)$$

27

465  Let $s = j\omega$, we are able to obtain the matrix form of the forced response in terms of angular frequency $\omega$:

$$\begin{bmatrix} X_1(j\omega) \\ X_2(j\omega) \\ X_3(j\omega) \end{bmatrix} = \mathbf{H} \begin{bmatrix} F_1(j\omega) \\ F_2(j\omega) \\ F_3(j\omega) \end{bmatrix} \tag{A.10}$$

where

$$\mathbf{H} = \begin{bmatrix} H_{11}(j\omega) & H_{12}(j\omega) & H_{13}(j\omega) \\ H_{21}(j\omega) & H_{22}(j\omega) & H_{23}(j\omega) \\ H_{31}(j\omega) & H_{32}(j\omega) & H_{33}(j\omega) \end{bmatrix} \tag{A.11}$$

By applying Mason's rule [36] to the block diagram shown in Fig. 5, we are able to obtain the following:

$$H_{11}(j\omega) = \frac{H_2(j\omega)H_3(j\omega) - K_c^2}{D(j\omega)} \tag{A.12}$$

$$H_{22}(j\omega) = \frac{H_1(j\omega)H_3(j\omega)}{D(j\omega)} \tag{A.13}$$

$$H_{33}(j\omega) = \frac{H_1(j\omega)H_2(j\omega) - K_c^2}{D(j\omega)} \tag{A.14}$$

$$H_{12}(j\omega) = H_{21}(j\omega) = \frac{H_3(j\omega)K_c}{D(j\omega)} \tag{A.15}$$

$$H_{23}(j\omega) = H_{32}(j\omega) = \frac{H_1(j\omega)K_c}{D(j\omega)} \tag{A.16}$$

$$H_{13}(j\omega) = H_{31}(j\omega) = \frac{K_c^2}{D(j\omega)} \tag{A.17}$$

470  where

$$\begin{aligned} D(j\omega) = {} & H_1(j\omega)H_2(j\omega)H_3(j\omega) \\ & - \left[ H_1(j\omega) + H_3(j\omega) \right] K_c^2 \end{aligned} \tag{A.18}$$

28

## Appendix B. Transfer function ratio approximations of out-of-phase mode

We make the following assumptions as in the text: a quality factor of $Q = 2 \times 10^4$, $|K/K_c| = 200$, $K_2/K = 2$, $\gamma_3 = 40000$, the sensor is perturbed by $|\Delta K/K| = 5/\gamma_3$. Near the out-of-phase mode frequency:

$$\omega \approx \sqrt{\frac{1}{M}\left[K + K_c + \frac{1}{2}(\Delta K - \alpha + \sqrt{\Delta K^2 + \alpha^2})\right]} \qquad \text{(B.1)}$$

Since $H_{13} = H_{31}$, the ratio $|H_{11}^2/H_{13}^2|$ near the out-of-phase mode frequency can be approximated using Eq. (10):

$$\left|\frac{H_{11}^2}{H_{13}^2}\right| \approx \left|-\frac{\sqrt{\gamma_3^2(\Delta K/K)^2 + 4} - \gamma_3(\Delta K/K)}{2} + j\frac{\gamma_3}{Q}\right|^2 = 30.96 \qquad \text{(B.2)}$$

Now consider the ratio $|H_{12}^2/H_{13}^2|$ near the out-of-phase mode frequency:

$$\left|\frac{H_{12}^2}{H_{13}^2}\right| \approx \left|\frac{H_3(j\omega_{op})}{K_c}\right|^2 \qquad \text{(B.3)}$$

Let $s = j\omega$ in $H_3$ in Eq. (A.9) and substitute into Eq. (B.3):

$$\left|\frac{H_{12}^2}{H_{13}^2}\right| \approx \left|\frac{\Delta K}{K_c} + \frac{K_c}{K_2 - K + K_c} + j\frac{K + K_c}{QK_c}\right|^2 = 7.51 \times 10^{-4} \qquad \text{(B.4)}$$

Therefore, $|H_{12}^2|/|H_{11}^2| = 2.43 \times 10^{-5}$. So we are able to conclude that $|H_{12}|^2$ and $|H_{13}|^2$ are both negligible compared to $|H_{11}|^2$.

## References

[1] G. Binnig, C. Quate, C. Gerber, Atomic force microscope, Phys. Rev. Lett. 56 (1986) 930–933. `doi:10.1103/PhysRevLett.56.930`.

[2] M. Nonnenmacher, M. oBoyle, H. Wickramasinghe, Kelvin probe force microscopy, Applied Physics Letters 58 (25) (1991) 2921–2923. `doi: 10.1063/1.105227`.

29

[3] K. Autumn, Y. A. Liang, S. T. Hsieh, W. Zesch, W. P. Chan, T. W. Kenny, R. Fearing, R. J. Full, Adhesive force of a single gecko foot-hair, Nature 405 (6787) (2000) 681–685. doi:10.1038/35015073.

[4] K. Kim, J. Cheng, Q. Liu, X. Y. Wu, Y. Sun, Investigation of mechanical properties of soft hydrogel microcapsules in relation to protein delivery using a mems force sensor, Journal of Biomedical Materials Research Part A 92 (1) (2010) 103–113. doi:10.1002/jbm.a.32338.

[5] A. Seshia, M. Palaniapan, T. Roessig, R. Howe, R. Gooch, T. Schimert, S. Montague, A vacuum packaged surface micromachined resonant accelerometer, Microelectromechanical Systems, Journal of 11 (6) (2002) 784–793. doi:10.1109/JMEMS.2002.805207.

[6] F. Beyeler, A. Neild, S. Oberti, D. J. Bell, Y. Sun, J. Dual, B. J. Nelson, Monolithically fabricated microgripper with integrated force sensor for manipulating microobjects and biological cells aligned in an ultrasonic field, Microelectromechanical Systems, Journal of 16 (1) (2007) 7–15. doi:10.1109/JMEMS.2006.885853.

[7] M. Li, E. J. Ng, V. A. Hong, C. H. Ahn, Y. Yang, T. W. Kenny, D. A. Horsley, Single-structure 3-axis lorentz force magnetometer with sub-30 nt/$\sqrt{\text{hz}}$ resolution, in: Micro Electro Mechanical Systems (MEMS), 2014 IEEE 27th International Conference on, IEEE, 2014, pp. 80–83. doi:10.1109/MEMSYS.2014.6765578.

[8] G. Stemme, Resonant silicon sensors, Journal of Micromechanics and Microengineering 1 (2) (1991) 113. doi:10.1088/0960-1317/1/2/004.

[9] H. A. Tilmans, M. Elwenspoek, J. H. Fluitman, Micro resonant force gauges, Sensors and Actuators A: Physical 30 (12) (1992) 35 – 53. doi:10.1016/0924-4247(92)80194-8.

[10] M. Spletzer, A. Raman, A. Q. Wu, X. Xu, R. Reifenberger, Ultrasensitive

30

515   mass sensing using mode localization in coupled microcantilevers, Applied
      Physics Letters 88 (25) (2006) 1 – 3. doi:10.1063/1.2216889.

[11]  P. Anderson, Absence of diffusion in certain random lattices, Phys. Rev.
      109 (1958) 1492–1505. doi:10.1103/PhysRev.109.1492.

[12]  P. Thiruvenkatanathan, J. Yan, J. Woodhouse, A. Seshia, Enhancing para-
520   metric sensitivity in electrically coupled mems resonators, Microelectrome-
      chanical Systems, Journal of 18 (5) (2009) 1077–1086.  doi:10.1109/
      JMEMS.2009.2025999.

[13]  P. Thiruvenkatanathan, A. Seshia, Mode-localized displacement sensing,
      Microelectromechanical Systems, Journal of 21 (5) (2012) 1016–1018. doi:
525   10.1109/JMEMS.2012.2198047.

[14]  M. Manav, G. Reynen, M. Sharma, E. Cretu, A. S. Phani, Ultrasensi-
      tive resonant mems transducers with tuneable coupling, Journal of Mi-
      cromechanics and Microengineering 24 (5) (2014) 055005. doi:10.1088/
      0960-1317/24/5/055005.

530   [15]  C. Zhao, G. Wood, J. Xie, H. Chang, S. Pu, M. Kraft, A three degree-of-
      freedom weakly coupled resonator sensor with enhanced stiffness sensitivity,
      submitted.

[16]  P. Thiruvenkatanathan, J. Yan, A. Seshia, Ultrasensitive mode-localized
      micromechanical electrometer, in: Frequency Control Symposium (FCS),
535   2010 IEEE International, 2010, pp. 91–96.  doi:10.1109/FREQ.2010.
      5556368.

[17]  P. Thiruvenkatanathan, J. Yan, A. Seshia, Common mode rejection in elec-
      trically coupled mems resonators utilizing mode localization for sensor ap-
      plications, in: Frequency Control Symposium, 2009 Joint with the 22nd
540   European Frequency and Time forum. IEEE International, 2009, pp. 358–
      363. doi:10.1109/FREQ.2009.5168201.

31

[18] T. R. Albrecht, P. Grtter, D. Horne, D. Rugar, Frequency modulation detection using high q cantilevers for enhanced force microscope sensitivity, Journal of Applied Physics 69 (2) (1991) 668–673. doi:10.1063/1.347347.

[19] R. W. Carpick, M. Salmeron, Scratching the surface: fundamental investigations of tribology with atomic force microscopy, Chemical Reviews 97 (4) (1997) 1163–1194. doi:10.1021/cr960068q.

[20] A. Stalder, U. Drig, Nanoguitar: Oscillating string as force sensor, Review of Scientific Instruments 66 (6) (1995) 3576–3579. doi:10.1063/1.1145472.

[21] T. D. Stowe, K. Yasumura, T. W. Kenny, D. Botkin, K. Wago, D. Rugar, Attonewton force detection using ultrathin silicon cantilevers, Applied Physics Letters 71 (2) (1997) 288–290. doi:10.1063/1.119522.

[22] M. Manav, Vibration mode localization in coupled microelectromechanical resonators, Master's thesis, The University of British Columbia, Vancouver, Canada (2014).

[23] C. Zhao, G. Wood, J. Xie, H. Chang, S. Pu, M. Kraft, A sensor for stiffness change sensing based on three weakly coupled resonators with enhanced sensitivity, in: Micro Electro Mechanical Systems (MEMS), 2015 IEEE 28th International Conference on, IEEE, 2015, pp. 881–884.

[24] J. A. Harley, T. W. Kenny, A high-stiffness axial resonant probe for atomic force microscopy, Microelectromechanical Systems, Journal of 10 (3) (2001) 434–441. doi:10.1109/84.946802.

[25] V. Kaajakari, Practical MEMS, 1st Edition, Small Gear Publishing, Las Vegas, NV, 2009.

[26] S. Timoshenko, Vibration Problems in Engineering, 4th Edition, Wiley, New York, 1974.

32

[27] T. A. W. Roessig, Integrated MEMS Tuning Fork Oscillations for Sensor Applications, Ph.D. thesis, University of California, Berkeley (1998).

570 [28] C.-C. Nguyen, Frequency-selective mems for miniaturized low-power communication devices, Microwave Theory and Techniques, IEEE Transactions on 47 (8) (1999) 1486–1503. doi:10.1109/22.780400.

[29] R. C. Elandt-Johnson, Survival models and data analysis, Vol. 110, John Wiley & Sons, 1980.

575 [30] T. Gabrielson, Mechanical-thermal noise in micromachined acoustic and vibration sensors, Electron Devices, IEEE Transactions on 40 (5) (1993) 903–909. doi:10.1109/16.210197.

[31] P. Thiruvenkatanathan, J. Woodhouse, J. Yan, A. A. Seshia, Limits to mode-localized sensing using micro- and nanomechanical resonator arrays, 580 Journal of Applied Physics 109 (10) (2011) 1 – 11. doi:10.1063/1. 3590143.

[32] P. Saulson, Thermal noise in mechanical experiments, Phys. Rev. D 42 (1990) 2437–2445. doi:10.1103/PhysRevD.42.2437.

[33] K. Wang, C.-C. Nguyen, High-order micromechanical electronic filters, in: 585 Micro Electro Mechanical Systems, 1997. MEMS '97, Proceedings, IEEE., Tenth Annual International Workshop on, 1997, pp. 25–30. doi:10.1109/ MEMSYS.1997.581759.

[34] M. V. Salapaka, H. S. Bergh, J. Lai, A. Majumdar, E. McFarland, Multi-mode noise analysis of cantilevers for scanning probe microscopy, Journal 590 of Applied Physics 81 (6) (1997) 2480–2487. doi:10.1063/1.363955.

[35] J. B. Xie, Y. C. Hao, H. L. Chang, W. Z. Yuan, Single mask selective release process for complex soi mems device, Key Engineering Materials 562 (2013) 1116–1121. doi:10.4028/www.scientific.net/KEM.562-565.1116.

33

[36] S. Mason, Feedback Theory-Some Properties of Signal Flow Graphs,
595     Vol. 41, 1953. `doi:10.1109/JRPROC.1953.274449`.

34

Table 3: Design parameters of the device

| Parameter | Design Value | Unit |
|---|---|---|
| Device layer thickness | 30 | $\mu$m |
| Suspension beam lengths ($L$) (resonator 1, 2 and 3) | 300 | $\mu$m |
| Suspension beam width ($w$) (resonator 1 and 3) | 4 | $\mu$m |
| Suspension beam width ($w_2$) (resonator 2) | 5 | $\mu$m |
| Tether length ($L_t$) | 170 | $\mu$m |
| Tether width ($w_t$) | 5 | $\mu$m |
| Air gaps ($d = d_c = d_b$) | 3.5 | $\mu$m |
| Air gaps ($d_e$) | 4.5 | $\mu$m |
| Cross-sectional area ($A = A_c = A_b$) | $360 \times 22$ | $(\mu$m$)^2$ |
| Cross-sectional area ($A_e$) | $160 \times 22$ | $(\mu$m$)^2$ |
| Cross-sectional area ($A_{cf}$) | $70 \times 22$ | $(\mu$m$)^2$ |
| Sensing transduction factor ($\eta_s$) (12V coupling voltage) | $4.01 \times 10^{-8}$ | A/(m $\cdot$ rad/s) |
| Actuation transduction factor ($\eta_t$) (12V coupling voltage) | $6.87 \times 10^{-8}$ | A/(m $\cdot$ rad/s) |
| Proof mass ($M$) | $6.87 \times 10^{-9}$ | kg |
| Resonant frequency (single resonator) | 13.24 | kHz |

35

Table 4: Sensitivity comparison with state-of-the-art resonant force sensors

| Reference | Type | Sensitivity expression | Sensitivity (/N) |
|-----------|------|------------------------|------------------|
| [5] | 1DoF resonator with differential sensing and leverage | $\dfrac{\partial(\Delta f/f)}{\partial T}$ | 8995 |
| [16] | 2DoF resonant sensor | $\dfrac{\partial(\text{Eigenstates shift})}{\partial T}$ | 1478 |
| Our work | 3DoF resonator sensor | $\dfrac{\partial(\text{Amplitude ratio})}{\partial T}$ | $4.9 \times 10^6$ |

Table 5: Theoretical noise evaluation of the 3DoF sensor

| Noise type | Measured signal power | Evaluated SNR (dB) | Evaluated Noise power |
|------------|----------------------|--------------------|-----------------------|
| Mechanical noise (resonator 1) | 0.53 (V$^2$) | 84.80 | $1.76 \times 10^{-9}$ (V$^2$) |
| Mechanical noise (resonator 3) | $1.60 \times 10^{-2}$ (V$^2$) | 84.80 | $5.30 \times 10^{-11}$ (V$^2$) |
| Electrical noise (resonator 1) | 0.53 (V$^2$) | 87.18 | $1.02 \times 10^{-9}$ (V$^2$) |
| Electrical noise (resonator 3) | $1.60 \times 10^{-2}$ (V$^2$) | 71.98 | $1.02 \times 10^{-9}$ (V$^2$) |
| Amplitude ratio noise | 33.11 | 71.72 | $2.23 \times 10^{-6}$ |

36